

Visible Light Positioning With Lamé Curve LEDs: A Generic Approach for Camera Pose Estimation

Wenxuan Pan[✉], *Graduate Student Member, IEEE*, Yang Yang, *Senior Member, IEEE*, Dong Wei, Zhiyu Zhu, Jintao Wang, Huan Wu, and Yao Nie

Abstract—Camera-based visible light positioning (VLP) is a promising technique for accurate and low-cost indoor camera pose estimation (CPE). To reduce the number of required light-emitting diodes (LEDs), advanced methods commonly exploit LED shape features for positioning. Although interesting, they are typically restricted to a single LED geometry, leading to failure in heterogeneous LED-shape scenarios. To address this challenge, this paper investigates Lamé curves as a unified representation of common LED shapes and proposes a generic VLP algorithm using Lamé curve-shaped LEDs, termed LC-VLP. In the considered system, multiple ceiling-mounted Lamé curve-shaped LEDs periodically broadcast their curve parameters via visible light communication, which are captured by a camera-equipped receiver. Based on the received LED images and curve parameters, the receiver can estimate the camera pose using LC-VLP. Specifically, an LED database is constructed offline to store the curve parameters, while online positioning is formulated as a nonlinear least-squares problem and solved iteratively. To provide a reliable initialization, a correspondence-free perspective- n -points (FreePnP) algorithm is further developed, enabling approximate CPE without any pre-calibrated reference points. The performance of LC-VLP is verified by both simulations and experiments. Simulations show that LC-VLP outperforms state-of-the-art methods in both circular- and rectangular-LED scenarios, achieving reductions of over 40% in position error and 25% in rotation error. Experiments further show that LC-VLP can achieve an average position accuracy of less than 4 cm.

Index Terms—Camera pose estimation, Lamé curve, nonlinear optimization, visible light positioning (VLP).

I. INTRODUCTION

INDOOR positioning has become a fundamental enabling technology for a wide range of location-aware applications in smart buildings, robotics, and the Internet of Things (IoT). Although the global navigation satellite systems (GNSSs) are predominant and well-established solutions that can provide reliable positioning performance in outdoor scenarios, they

Received 2 February 2026. This work was supported in part by the National Natural Science Foundation of China under Grant 62371065 and Grant 61871047, and in part by BUPT Innovation and Entrepreneurship Support Program under Grant 2025-YC-S007. (Corresponding author: Yang Yang.)

Wenxuan Pan and Yang Yang are with Beijing Key Laboratory of Network System Architecture and Convergence, School of Information and Communication Engineering, Beijing University of Posts and Telecommunications, Beijing 100876, China (e-mail: pwx@bupt.edu.cn; yangyang01@bupt.edu.cn).

Dong Wei is with the Institute of Information Engineering, Chinese Academy of Sciences, Beijing 100085, China (e-mail: weidong@iie.ac.cn).

Zhiyu Zhu is with the College of Physics and Electronic Engineering, Shanxi University, Taiyuan 030006, China (e-mail: zhiyu.zhu@sxu.edu.cn).

Jintao Wang, Huan Wu, and Yao Nie are with the School of Electronic and Information Engineering, West Anhui University, Lu'an 237012, China (e-mail: wangjintao5678@163.com; wuhuan@wxc.edu.cn; nieyao@wxc.edu.cn).

Color versions of one or more figures in this article are available at [xxx](#).
Digital Object Identifier [xxx](#)

face challenges indoors, including severe signal attenuation and degraded reliability [1], [2]. Under this background, a variety of indoor positioning technologies have been developed, such as WiFi [3], Bluetooth low energy (BLE) [4], ultra-wideband (UWB) [5], radio frequency identification (RFID) [6], and visible light positioning (VLP) [7], [8], [9], [10], [11], [12], [13]. Among these, the VLP technology has attracted increasing attention, as it can achieve high accuracy while leveraging existing lighting infrastructure at a low cost [14].

VLP systems employ light-emitting diodes (LEDs) as transmitters, which periodically broadcast data packets containing essential information, such as the LED identities (IDs) via visible light communication (VLC). To receive these signals, two types of receivers are commonly used: Photodiodes (PDs) [7], [8], [9] and cameras [10], [11], [12], [13], each with its own advantages and limitations [14], [15], [16]. Camera-based methods typically utilize complementary metal-oxide-semiconductor (CMOS) cameras to capture images of LED luminaires. By exploiting the rolling-shutter effect (RSE), the LED IDs can be detected and decoded, while visual features extracted from the captured images can be jointly used for 6-degrees of freedom (DoF) camera pose estimation (CPE). Besides their strong robustness to ambient light interference [11], camera-based methods leverage the ubiquitous availability of cameras which support a wide range of applications beyond positioning. Consequently, camera-based methods are regarded as practical, flexible, and easy to integrate into existing systems [14], [15]. However, achieving high-accuracy VLP with fewer LEDs while maintaining robustness across heterogeneous LED shapes remains a challenging open problem.

A. Related Works

Existing camera-based VLP methods can generally be categorized into two classes: Point-source-based methods [17], [18] and planar-source-based methods [10], [11], [19], [20], [21], [22], [23], [24]. Point-source-based methods exploit only the centroids of LED projections and its positioning process can be formulated as a perspective- n -points (PnP) problem [25], [26], [27] when multiple LEDs are visible. However, the requirement of observing ≥ 4 LEDs imposes strict constraints on LED deployment density [28]. Although auxiliary sensors such as inertial measurement units (IMUs) can be introduced to reduce the number of required LEDs [18], they inevitably increase system complexity and hardware cost.

In contrast, planar-source-based methods explicitly exploit the geometric shape of LEDs for positioning. By incorporat-

ing fine-grained shape information, these methods typically require fewer visible LEDs, and have therefore become the dominant paradigm. However, existing studies are usually restricted to a single specific LED shape, such as circular LEDs [10], [11], [19], [20], [21] or rectangular LEDs [22], [23], [24]. The works in [10], [11] and [19] proposed VLP approaches that leverage the geometric characteristics of circular LEDs without other auxiliary sensors. Specifically, Zhang et al. [19] adopted a weak-perspective projection model which guarantees solution uniqueness at the cost of reduced accuracy. To overcome this limitation, Zhu et al. [10] employed the pinhole projection model and resolved the inherent ambiguity by exploiting an additional visible LED. They further introduced the visual odometry (VO) [11] to enable positioning with a single circular LED under dynamic camera motion scenarios. For rectangular LEDs, Bai et al. [22] proposed using the perspective-4-line (P4L) algorithm for CPE. However, this approach requires VLC information to be transmitted at a specific LED corner, which is difficult to implement on commercial off-the-shelf rectangular luminaires [29]. Moreover, the works in [20], [21], [23] and [24] introduced additional IMUs or magnetometers to assist in CPE. As discussed earlier, such auxiliary sensors not only increase hardware complexity but also suffer from degraded reliability under electromagnetic interferences, thereby limiting their practical applicability. To summarize, although the above works [10], [11], [19], [20], [21], [22], [23], [24] exploit LED shape feature for positioning, they are restricted to a single specific LED geometry, and thus they fail in heterogeneous LED-shape scenarios or when other common LED shapes, e.g., rhombic or elliptical LEDs, are deployed. Moreover, these methods rely on purely geometric solutions, which are sensitive to image noises since the camera pose is not refined through global iterative optimization.

Motivated by the above limitations, a unified representation that can characterize diverse planar LED shapes is highly desirable. *Lamé curves* [30], [31], [32], also referred to as the *superellipses*, constitute a general family of parametric curves that naturally subsume common LED shapes as special cases. Introducing Lamé curves into VLP can enable a unified framework that accommodates multiple LED shapes within a single algorithm. Nevertheless, this generality comes at the cost of more complex curve equations, which renders conventional purely geometric methods inapplicable. Therefore, exploiting Lamé curve LEDs for VLP deserves further investigation.

B. Contributions

The primary contribution of this paper is a generic VLP algorithm based on Lamé curve-shaped LEDs, termed LC-VLP. *To the authors' best knowledge, this is the first generic VLP approach that unifies the modeling of various commonly-used LED shapes and achieves full 6-DoF CPE.* Our key contributions are summarized as follows:

- We investigate a unified representation for commonly-used LED shapes, namely Lamé curves. For the first time, Lamé curves are introduced into VLP to provide a unified parametric modeling that naturally covers a wider range of planar LED geometries, including circular, rectangular,

rhombic, and elliptical shapes. To accommodate shape diversity, an LED database construction method is further developed to associate each LED with its corresponding Lamé-curve parameters, enabling a single unified framework without algorithm switching.

- Based on the Lamé-curve modeling of LEDs with different shapes, we propose a generic LC-VLP algorithm that achieves higher accuracy and robustness in heterogeneous and mixed LED deployments. Specifically, LC-VLP is built upon a *back-projection strategy*, where the LED projection points are back-projected onto the ceiling plane. A nonlinear least-squares (NLLS) optimization model is then formulated, where iterative refinement is performed to jointly exploit all observed LED contours for accurate 6-DoF CPE.
- The NLLS optimization requires a reliable initial estimate to ensure convergence. To this end, we propose a correspondence-free PnP (FreePnP) algorithm. Unlike conventional PnP methods, FreePnP does not require prior knowledge of pre-calibrated 3D–2D reference point (RP) correspondences, yet it is still capable of coarse CPE. Specifically, we theoretically prove a *collinearity invariance theorem*. Based on this theorem and an assumption of uniform distribution of LED contour points, multiple approximate virtual correspondences can be constructed. The camera pose is initialized by applying a PnP solver to these virtual correspondences.

Substantial simulation results show that LC-VLP outperforms state-of-the-art (SoTA) methods in both circular- and rectangular-LED scenarios, achieving reductions of over 40% in position error and 25% in rotation error. We further implement LC-VLP by developing an experimental prototype in a practical scenario. Based on this prototype, experiments are implemented, which show that LC-VLP can achieve an average position accuracy of less than 4 cm.

C. Notations and Paper Organization

In this paper, matrices and column vectors are denoted by uppercase and lowercase boldface, e.g., \mathbf{R} and \mathbf{v} , respectively, with $(\cdot)^\top$ denoting their transposition. For vector \mathbf{v} , $\|\mathbf{v}\|$ represents its Euclidean norm, and $\tilde{\mathbf{v}} \triangleq [\mathbf{v}^\top, 1]^\top$ denotes its homogeneous representation. For square matrix \mathbf{R} , $\det(\mathbf{R})$ and $\text{tr}(\mathbf{R})$ denote its determinant and trace, respectively. Sets are denoted by calligraphic uppercase letters, e.g., \mathcal{A} , with $|\mathcal{A}|$ indicating its cardinality, and $\{a_i\}_{i=1}^N$ denoting a sequence. Points are represented by uppercase letters such as P , and $\overline{P_1P_2}$ denotes the segment connecting points P_1 and P_2 .

The rest of the paper is organized as follows. Section II introduces the system model. In Section III, the proposed FreePnP and LC-VLP algorithms are presented in detail. Then, Section IV presents the simulation and experimental setup and results. Finally, Section V concludes this paper.

II. SYSTEM MODEL AND PROBLEM FORMULATION

A. System Model

The considered typical indoor VLP scenario is illustrated in Fig. 1. In this scenario, multiple Lamé curve-shaped LEDs are



Fig. 1. The considered VLP scenario.

installed in the ceiling. These LEDs function as transmitters that continuously broadcast VLC information while providing illumination. In practical environments, such LEDs often exhibit heterogeneous shapes due to mixed lighting infrastructures, e.g., circular downlights combined with rectangular panel lights in offices, or the coexistence of legacy luminaires and newly retrofitted LED fixtures in shopping malls and transportation hubs. The positioning device is equipped with a camera capable of simultaneously receiving both VLC signals and visual information from the LEDs, thereby enabling real-time, onboard estimation of its own 6-DoF pose. In particular:

1) *Lamé Curve-Shaped LEDs*: Lamé curves [30], [31], [32] are commonly used as design elements, particularly in the shapes of LED luminaires. On the plane xOy , consider a Lamé curve with center $(x_0, y_0)^\top$. Its major and minor axes are aligned with the x - and y -axes, with lengths $2a$ and $2b$, respectively, and its order is denoted by γ . Then, the equation of this curve is given by:

$$\left| (x - x_0)/a \right|^{\gamma} + \left| (y - y_0)/b \right|^{\gamma} = 1. \quad (1)$$

The order γ determines the geometric shape of this curve:

- When $\gamma = 1$, the curve becomes a rhombus, and in the special case $a = b$, it reduces to a square (with vertices lying on the coordinate axes).
- When $\gamma = 2$, the curve becomes an ellipse, and in the special case $a = b$, it reduces to a circle.
- As $\gamma \rightarrow +\infty$, the curve approaches a rectangle, and in the special case $a = b$, it reduces to a square. In practice, a sufficiently large value of γ , such as 100 or larger, can be used to obtain an accurate approximation.

The Lamé curve formulation in (1) can provide a unified representation for common LED shapes such as circles [10] and rectangles [22]. This unification establishes the theoretical foundation for the proposed generic LC-VLP algorithm.

2) *Projection Model*: As shown in Fig. 2, we adopt the pinhole projection model [33] to describe the camera imaging process. First, we establish the following coordinate systems: (i) the 3D world coordinate system (WCS) $O-xyz$, (ii) the 3D camera coordinate system (CCS) $C-x^c y^c z^c$, and (iii) the 2D pixel coordinate system (PCS) $u^P O^P v^P$. Among these, in WCS, the z -axis points vertically upward toward the ceiling. The origin of CCS C coincides with the camera's optical center; Moreover, to ensure visibility of the LEDs, the z^c -axis is oriented approximately upward and is perpendicular to

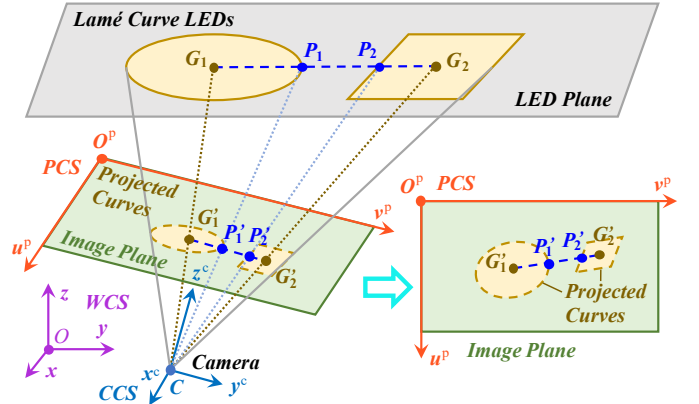


Fig. 2. The system projection diagram.

the image plane. The PCS lies on the image plane, and in 3D space, its u^P - and v^P -axes are parallel to the x^c - and y^c -axes of CCS, respectively. In the following, the coordinates of a point expressed in the WCS/CCS/PCS are referred to as its world/camera/pixel coordinates.

Consider a 3D point \mathbf{x}^c in CCS, whose projection onto the image plane yields a 2D image point \mathbf{u}^p . This projection process can be modeled as:

$$z^c \tilde{\mathbf{u}}^p = \mathbf{K} \mathbf{x}^c, \quad (2)$$

where $\mathbf{K} \triangleq \begin{bmatrix} f_x & 0 & u_0 \\ 0 & f_y & v_0 \\ 0 & 0 & 1 \end{bmatrix}$ is the intrinsic matrix of camera C which can be calibrated in advance. In matrix \mathbf{K} , f_x and f_y are the focal lengths in pixels; and $(u_0, v_0)^\top$ represent the pixel coordinates of the principal point.

We further consider the transformation between CCS and WCS. Since the two coordinate systems share the same scale, the relationship between the world coordinates x of a point in 3D space and its camera coordinates x^c is given by:

$$x^c = Rx + t, \quad (3)$$

where $R \in \mathfrak{SO}(3)$ is the rotation matrix representing the camera's orientation, $\mathfrak{SO}(3)$ represents the 3D special orthogonal group, and $t \in \mathbb{R}^3$ is the translation vector representing the camera's position offset. Matrix R and vector t constitute the camera extrinsics.

B. Problem Formulation

The camera's 6-DoF pose includes its world coordinates \mathbf{c} and its 3D rotation matrix \mathbf{R} . The objective of this work is to estimate this 6-DoF pose, given the pre-calibrated intrinsic matrix \mathbf{K} , the world-coordinate Lamé curve equations \mathcal{E}_i of the N observed LEDs (for $i = 1, \dots, N$), and the corresponding sets of pixel-coordinate projection points \mathcal{I}_i on the image plane. Moreover, if additional pre-calibrated RPs are available, these RPs can be incorporated to further assist the positioning process. We denote the set of world coordinates of these RPs and the set of their corresponding pixel-coordinate projection points as \mathcal{M} and \mathcal{M}' , respectively.

Based on the aforementioned system model, the camera optical center coincides with the origin of CCS. In the field of computer vision, it is common to use the optical center as the

representation of the camera [33]; thus, the camera coordinate of camera C is simply $\mathbf{0}$. Substituting $\mathbf{c}^c = \mathbf{0}$ into (3) yields:

$$\mathbf{c} = -\mathbf{R}^\top \mathbf{t}, \quad (4)$$

from which we can see that estimating the world coordinates of camera C is equivalent to solving for the extrinsics \mathbf{R} and \mathbf{t} . Accordingly, we formulate the positioning process as:

$$\mathbf{R}, \mathbf{t} = \mathbf{f}(\{\mathcal{I}_i\}_{i=1}^N, \mathcal{M}'; \{\mathcal{E}_i\}_{i=1}^N, \mathcal{M}) \quad (5)$$

$$\text{s.t. } \mathbf{R} \in \mathfrak{SO}(3), \mathbf{t} \in \mathbb{R}^3, -\mathbf{R}^\top \mathbf{t} \in \mathcal{U}. \quad (5a)$$

In (5), the function $\mathbf{f}(\cdot)$ denotes the mapping used to compute the extrinsics. In (5a), the constraints $\mathbf{R} \in \mathfrak{SO}(3)$ and $\mathbf{t} \in \mathbb{R}^3$ specify the admissible forms of the rotation matrix and translation vector, respectively, while the constraint $-\mathbf{R}^\top \mathbf{t} \in \mathcal{U}$ ensures that the estimated camera position lies within a predefined feasible region \mathcal{U} , e.g., not above the ceiling or outside the indoor environment, etc.

To address problem (5), we propose an LC-VLP algorithm that enables a generic and unified solution for camera position and orientation estimation with Lamé curve-shaped LEDs of arbitrary order. The details of the proposed algorithm are presented in the following sections.

III. GENERIC VLP WITH LAMÉ CURVE LEDs

This section presents the proposed LC-VLP method. First, a database of Lamé curve-shaped LEDs is constructed, and a local auxiliary coordinate system is defined for each LED. Then, leveraging the proposed projection collinearity invariance theorem, a FreePnP algorithm is developed to provide an initial estimate of the camera 6-DoF pose without requiring sufficient pre-calibrated 3D–2D RP correspondences. Finally, a back-projection strategy is adopted to formulate an NLLS optimization model, which is solved using nonlinear optimization methods. The computational complexity of LC-VLP is also analyzed. Detailed descriptions are provided below.

A. LED Database Construction

In the considered scenario, the positions, shapes, and sizes of the Lamé curve-shaped LEDs may differ from each other. Consequently, an LED database should be constructed in advance to store these parameters. When positioning, the parameters of the captured LEDs are received by the CMOS camera via VLC and RSE [10], [11].

In WCS, assume there are N' LEDs on the ceiling plane, whose equation is $z = z_0$. The boundary curve of the i -th LED is denoted by \mathcal{E}_i , $1 \leq i \leq N'$, and its center is $\bar{\mathbf{x}}_i = (\bar{x}_i, \bar{y}_i, z_0)^\top$. Then, the equation of \mathcal{E}_i is given by:

$$\begin{cases} |(x - \bar{x}_i)/a_i|^{\gamma_i} + |(y - \bar{y}_i)/b_i|^{\gamma_i} = 1, \\ z = z_0. \end{cases} \quad (6a)$$

that of WCS. Under this transformation, the equation of LED curve \mathcal{E}_i becomes:

$$\begin{bmatrix} x \\ y \\ z \end{bmatrix} = \begin{bmatrix} \bar{x}_i \\ \bar{y}_i \\ z_0 \end{bmatrix} + \rho_i(\theta) \begin{bmatrix} \cos \theta \\ \sin \theta \\ 0 \end{bmatrix} \triangleq \bar{\mathbf{x}}_i + \rho_i(\theta) \cdot \psi(\theta). \quad (7)$$

Substituting (7) into (6a), we can obtain:

$$\begin{cases} \rho_i(\theta) = (|\cos \theta|^{\gamma_i}/a_i^{\gamma_i} + |\sin \theta|^{\gamma_i}/b_i^{\gamma_i})^{-1/\gamma_i}, \\ z = z_0, \end{cases} \quad (8a)$$

$$(8b)$$

which are the equations of LED curve \mathcal{E}_i in CyCS.

Note that the Lamé curve in (6)–(8) assumes that its major axis is aligned with the x -axis of WCS. In practice, however, some Lamé curve-shaped LEDs may not satisfy this alignment. Even so, the proposed algorithm can readily accommodate such case. Suppose the angle between the major axis of the i -th LED curve \mathcal{E}_i and the x -axis of WCS is ϕ_i . We can then define a local WCS, denoted WCS_i , obtained by rotating the global WCS counterclockwise around the global z -axis by ϕ_i . Similarly, the corresponding CyCS _{i} can be obtained in the same manner. In CyCS _{i} , the curve \mathcal{E}_i assumes the form of (7) and (8). By rotating (8) back into the global CyCS, the resulting equation of \mathcal{E}_i is given by:

$$\mathbf{x}_i = \bar{\mathbf{x}}_i + \rho_i(\theta - \phi_i) \cdot \psi(\theta - \phi_i). \quad (9)$$

It is therefore evident that employing the CyCS as an auxiliary representation significantly simplifies the subsequent steps of the algorithm.

Based on the above analysis, the required parameters for each LED include the center $(\bar{x}_i, \bar{y}_i, z_0)^\top$, the major and minor axes a_i and b_i , the order γ_i , and the major-axis orientation ϕ_i . Accordingly, the LED database is constructed as:

$$\mathcal{D} = \{(\bar{x}_i, \bar{y}_i, a_i, b_i, \gamma_i, \phi_i)\}_{i=1}^{N'}. \quad (10)$$

B. Correspondence-Free PnP

In this subsection, our target is to obtain an initial estimate for the subsequent nonlinear optimization. Since the LEDs are Lamé curve-shaped rather than simply circular or rectangular, PnP methods [26], [27] become the primary candidates for generating such an initialization. However, as discussed earlier, PnP methods require ≥ 4 pre-calibrated RPs in the environment, and the 3D–2D correspondences must be known [28]. Although in typical VLP scenarios, the LED centers can be pre-calibrated [10], [11], relying solely on LED centers generally requires ≥ 4 LEDs to be simultaneously captured by the camera, which imposes a stringent constraint on the LED layout. To address this limitation, we propose the FreePnP method that approximates the solution without relying on enough explicit 3D–2D correspondences, but providing a reliable initialization for the subsequent stage.

First, if the LED centers are pre-calibrated, these 3D–2D correspondences can be directly used; otherwise, the centers of their projection curves can be used as approximations [10]. Then, we propose the following theorem:

Theorem 1 (Invariability of Collinearity): Under the pinhole projection model (2) and (3), given three distinct points on

a plane that does not contain the camera optical center, then these points are collinear in WCS *if and only if* their projected points on the image plane are collinear in PCS.

Proof: Please refer to Appendix A. \square

Remark 1: For clarity, we illustrate Theorem 1 in Fig. 2. Let the centers of LED₁ and LED₂ be denoted by G_1 and G_2 , respectively, and their projections on the image plane by G'_1 and G'_2 . Consider the point P_1 defined as the intersection between segment G_1G_2 and the boundary of LED₁. According to Theorem 1, the projection of this point, P'_1 , must lie on the segment $\overline{G'_1G'_2}$. Since P'_1 also lies on the projection curve of LED₁, it follows that P'_1 must be the intersection between the projection curve of LED₁ and $\overline{G'_1G'_2}$. Likewise, the point P'_2 must be the intersection between the projection curve of LED₂ and $\overline{G'_1G'_2}$. Consequently, we obtain two additional pairs of 3D–2D correspondences beyond the LED centers, i.e., (P_1, P'_1) and (P_2, P'_2) .

Then, we make the following assumption:

Assumption 1: The contour points extracted from the LED's projection curve are densely and approximately uniformly distributed with respect to (w.r.t.) the arc length.

Remark 2: Assumption 1 is reasonable since the projection of each LED can typically occupy a sufficiently large number of pixels. Under this condition, edge detection and contour extraction methods [34] are capable of producing dense and consecutive pixel samples along the boundary. Furthermore, by appropriately adjusting the camera exposure time, the contrast between the LED and the background can be significantly enhanced [10]. This can stabilize the edge detection process and consequently result in a contour point set that is more evenly distributed along the projected curve.

Assume that camera C captures the projections of N LEDs. Based on Theorem 1 and Assumption 1, we aim to sample point sets \mathcal{E}_i^b and \mathcal{I}_i^b from the boundary curve \mathcal{E}_i of LED _{i} and its projected contour point set \mathcal{I}_i , respectively, for applying a PnP-based initial estimation. Note that the points in \mathcal{E}_i^b and \mathcal{I}_i^b are expected to approximately satisfy the 3D–2D projection correspondences, thereby ensuring the estimation reliability.

We first aim to identify the 3D–2D correspondence (P_i, P'_i) described in Remark 1 for each LED _{i} . On the image plane, let the center of the projection of LED _{i} be denoted by \bar{u}_i . According to Remark 1, an additional LED _{i} is required to assist in determining (P_i, P'_i) ; without loss of generality, we set $\iota = (i \bmod N) + 1$. Then, from the contour point set \mathcal{I}_i , we select the pixel point \mathbf{u}_{i0}^p whose direction (w.r.t. \bar{u}_i) is closest to the vector $\bar{u}_\iota - \bar{u}_i$ as an approximation of P'_i :

$$\mathbf{u}_{i0}^p = \arg \min_{\mathbf{u} \in \mathcal{I}_i} \langle \mathbf{u} - \bar{u}_i, \bar{u}_\iota - \bar{u}_i \rangle, \quad (11)$$

where $\langle \cdot, \cdot \rangle$ represents the included angle between two vectors. In WCS, let the center of LED _{i} be denoted by $(\bar{x}_i, \bar{y}_i, z_0)^\top$. Similarly, the LED _{ι} is employed to assist in determining P_i . According to (9), the angle between the vector $(\bar{x}_\iota - \bar{x}_i, \bar{y}_\iota - \bar{y}_i, 0)^\top$ and the x_i -axis of WCS _{i} , i.e., the polar angle of P_i , is given by:

$$\beta_i = \text{atan}2(\bar{y}_\iota - \bar{y}_i, \bar{x}_\iota - \bar{x}_i) - \phi_i, \quad (12)$$

Consequently, the world coordinates of P_i is obtained by:

$$\mathbf{x}_{i0} = \bar{x}_i + \rho_i(\beta_i) \cdot \psi(\beta_i). \quad (13)$$

From the above analysis, we obtain a 3D–2D correspondence pair (P_i, P'_i) for each LED _{i} . However, we observe that as illustrated in Fig. 2, when $N = 2$, the four points G_1 , G_2 , P_1 , and P_2 are collinear, which is still insufficient to determine the extrinsics of camera C . Therefore, we further propose a contour sampling strategy to augment the set of approximate 3D–2D correspondences.

Specifically, in WCS, we uniformly sample the curve \mathcal{E}_i w.r.t. the polar angle measured from the LED center, and obtain the 3D sampled set \mathcal{E}_i^b . We take the polar angle β_i of P_i in WCS _{i} as the starting angle, and uniformly sample within the interval $[0, 2\pi]$ to obtain the following set of angles:

$$\Theta_i = \{\beta_i, \beta_i + \frac{1}{M}2\pi, \dots, \beta_i + \frac{M-1}{M}2\pi\} \bmod 2\pi. \quad (14)$$

Then, in a manner consistent with (13), the 3D sampling point set \mathcal{E}_i^b can be obtained as:

$$\mathcal{E}_i^b = \{\bar{x}_i + \rho_i(\theta) \cdot \psi(\theta) \mid \theta \in \Theta_i\}. \quad (15)$$

To obtain the corresponding 2D sampling set, we propose the following proposition:

Proposition 1: Uniform polar-angle sampling along the LED curve yields image projections that approximately correspond to uniform arc-length sampling on the projected contour.

Proof: Please refer to Appendix B. \square

According to Assumption 1, the extracted contour points are approximately uniformly distributed w.r.t. the arc length. Consequently, uniformly sampling these contour points is equivalent to approximately performing uniform arc-length sampling along the projected curve. Moreover, by Proposition 1, once a 3D–2D correspondence pair is determined as the starting points, uniform arc-length sampling on the projected curve corresponds to the projection of uniform polar-angle sampling on the original LED curve. Therefore, within \mathcal{I}_i , we assign the index 0 to \mathbf{u}_{i0}^p and re-index the remaining points in \mathcal{I}_i in a counterclockwise order. This \mathbf{u}_{i0}^p is recognized as the starting point. Then, we partition the points in \mathcal{I}_i evenly into M segments and select the following indices to form the sampling index set:

$$\mathcal{J}_i = \{0, \frac{1}{M}|\mathcal{I}_i|, \dots, \frac{M-1}{M}|\mathcal{I}_i|\}, \quad (16)$$

and thus, the 2D sampling set is defined as $\mathcal{I}_i^b = \{\mathbf{u}_{ij}^p\}_{j \in \mathcal{J}_i}$, which can be approximately regarded as the 2D projections of the 3D sampling point set \mathcal{E}_i^b .

Finally, for all N captured LEDs, we aggregate all the 3D sampling sets \mathcal{E}_i^b and the corresponding 2D sampling sets \mathcal{I}_i^b , and apply a PnP algorithm, such as the OPnP [27], to obtain an initial estimate of the camera extrinsics:

$$\mathbf{R}^{(0)}, \mathbf{t}^{(0)} = \text{PMNP}(\{\mathcal{E}_i^b\}_{i=1}^N, \{\mathcal{I}_i^b\}_{i=1}^N; \mathbf{K}). \quad (17)$$

The FreePnP algorithm is summarized in Algorithm 1. Note that in FreePnP, Assumption 1 and Proposition 1 introduce an approximation to the 3D–2D correspondences, which inevitably leads to estimation errors. However, these errors are typically within an acceptable range. Moreover, FreePnP is

Algorithm 1: FreePnP Algorithm

Input: For $1 \leq i \leq N$: LED curves \mathcal{E}_i ; LED centers $\bar{\mathbf{x}}_i$; Projected contour sets \mathcal{I}_i ; Projected LED centers $\bar{\mathbf{u}}_i$; Camera intrinsic matrix \mathbf{K} ;
Output: Estimate of camera extrinsics: $\mathbf{R}^{(0)}$ and $\mathbf{t}^{(0)}$.

1 **for** $i = 1 : N$ **do**
2 Calculate $\iota = (i \bmod N) + 1$;
3 Obtain an approximation of P'_i , \mathbf{u}_{i0}^p , by (11);
4 Calculate the starting polar angle β_i by (12);
5 Sample points by (14) and (15) to obtain the 3D set \mathcal{E}_i^b ;
6 Reorder \mathcal{I}_i counterclockwise with starting point \mathbf{u}_{i0}^p ;
7 Sample points by (16) to obtain the 2D set \mathcal{I}_i^b ;
8 Apply a PnP algorithm to $\{\mathcal{E}_i^b\}_{i=1}^N$ and $\{\mathcal{I}_i^b\}_{i=1}^N$ by (17);

only employed to provide an initial estimate of the camera extrinsics for the subsequent nonlinear optimization stage. Therefore, the overall accuracy of LC-VLP is not adversely affected. The nonlinear optimization-based refinement step will be detailed in the next subsection.

C. Nonlinear Optimization-Based Refinement

To refine the $\mathbf{R}^{(0)}$ and $\mathbf{t}^{(0)}$ obtained in Section III-B, a commonly adopted approach is to formulate a reprojection-based optimization model [13]. Conventional methods typically require ≥ 4 accurately known pairs of 3D–2D correspondences, and involve projecting 3D points onto the image plane. However, in the considered scenario it is generally not guaranteed that a sufficient number of exact 3D–2D correspondences are available. Moreover, directly projecting Lamé curves onto the image plane can result in complicated shape distortions, which makes it difficult to handle the optimization process.

To address these issues, we first propose a *back-projection strategy*, in which the 2D points on the image plane are back-projected onto the ceiling plane where the optimization is then carried out. On the image plane, for an LED projected point k' with pixel coordinate $\mathbf{u}_{k'}^p$, its back-projected point k in CCS can be obtained from (2) as:

$$\mathbf{x}_k^c = z_k^c \cdot (\mathbf{K}^{-1} \tilde{\mathbf{u}}_{k'}^p), \quad (18)$$

where z_k^c denotes the depth of point k in CCS and is unknown. Let $\mathbf{d}_k \triangleq \mathbf{K}^{-1} \tilde{\mathbf{u}}_{k'}^p$. Then, according to (3), the world coordinate of back-projected point k can be expressed as:

$$\hat{\mathbf{x}}_k = \mathbf{R}^T (\mathbf{x}_k^c - \mathbf{t}) = \mathbf{R}^T (z_k^c \mathbf{d}_k - \mathbf{t}). \quad (19)$$

We next solve for the depth z_k^c . Since the LEDs are mounted on the ceiling, the back-projected point k should lie on the ceiling plane, and thus its vertical coordinate in WCS satisfies $z_k = z_0$. Moreover, let $\mathbf{R} \triangleq [\mathbf{r}_1, \mathbf{r}_2, \mathbf{r}_3]$ which can be substituted into (19) and yields:

$$\mathbf{r}_3^T \cdot (z_k^c \mathbf{d}_k - \mathbf{t}) = z_0, \quad (20)$$

where the z_k^c is solved as:

$$z_k^c = \frac{z_0 + \mathbf{r}_3^T \cdot \mathbf{t}}{\mathbf{r}_3^T \cdot \mathbf{d}_k}. \quad (21)$$

Then, the back-projected point $\hat{\mathbf{x}}_k$ is obtained by substituting (21) into (19):

$$\hat{\mathbf{x}}_k = \mathbf{R}^T \left(\frac{z_0 + \mathbf{r}_3^T \cdot \mathbf{t}}{\mathbf{r}_3^T \cdot \mathbf{d}_k} \mathbf{d}_k - \mathbf{t} \right). \quad (22)$$

After obtaining the back-projected points, we further formulate an NLLS optimization model. Specifically, we define the *algebraic distance* [35] from point \mathbf{x} to Lamé curve \mathcal{E} as:

$$\varphi(\mathbf{x}, \mathcal{E}) = |(x - \bar{x})/a|^\gamma + |(y - \bar{y})/b|^\gamma - 1. \quad (23)$$

By definition, if \mathbf{x} lies on the curve \mathcal{E} , the algebraic distance $\varphi(\mathbf{x}, \mathcal{E}) = 0$; if \mathbf{x} lies inside \mathcal{E} , $\varphi(\mathbf{x}, \mathcal{E}) < 0$; otherwise, $\varphi(\mathbf{x}, \mathcal{E}) > 0$. Moreover, $\varphi(\mathbf{x}, \mathcal{E})$ can provide a coarse measure of the proximity between \mathbf{x} and \mathcal{E} .

In the absence of noise, the true camera extrinsics would cause all back-projected points $\hat{\mathbf{x}}_k$ to lie exactly on their corresponding LED curves \mathcal{E}_i , i.e., $\varphi(\hat{\mathbf{x}}_k, \mathcal{E}_i) = 0$, $\forall k' \in \mathcal{I}_i$. In practice, due to image noise and other interferences [10], [11], [13], the optimal extrinsics \mathbf{R}^* and \mathbf{t}^* can be obtained by minimizing the sum of squared algebraic distances from all back-projected points to their corresponding LED curves according to the LS principle. Therefore, we formulate the following NLLS optimization problem:

$$\arg \min_{\mathbf{R}, \mathbf{t}} \sum_{i=1}^N \sum_{k' \in \mathcal{I}_i} \varphi^2(\hat{\mathbf{x}}_k, \mathcal{E}_i) \quad (24)$$

$$\text{s.t. } \mathbf{R} \in \mathfrak{SO}(3), \mathbf{t} \in \mathbb{R}^3, -\mathbf{R}^T \mathbf{t} \in \mathcal{U}, \quad (24a)$$

$$\frac{1}{|\mathcal{M}|} \sum_{k' \in \mathcal{M}} \|\hat{\mathbf{x}}_k - \mathbf{x}_k\|^2 \leq \epsilon^2. \quad (24b)$$

Compared to (5), in (24b) we additionally consider the presence of pre-calibrated RPs on the ceiling. Let \mathcal{M} denote the set of their projected points on the image plane. These projected points are also back-projected onto the ceiling plane, and the mean squared back-projection error is constrained to be smaller than ϵ^2 . Incorporating this constraint can help eliminate potential ambiguous solutions [10] and accelerate the convergence of the iterative optimization.

In Problem (24), rotation matrix $\mathbf{R} \in \mathfrak{SO}(3)$ contains 9 parameters but has only 3 DoF. To simplify the optimization, we parameterize \mathbf{R} using the Rodrigues vector [36]. Let the Rodrigues vector of \mathbf{R} be denoted by $\boldsymbol{\omega} = \omega \mathbf{n}$, where \mathbf{n} is a unit vector. Then, by the *Rodrigues' Formula* [36], the rotation matrix can be expressed as:

$$\mathbf{R} = \mathbf{I} + [\mathbf{n}]_\times \sin \omega + ([\mathbf{n}]_\times)^2 (1 - \cos \omega), \quad (25)$$

where $[\mathbf{n}]_\times = \begin{bmatrix} 0 & -n_z & n_y \\ n_z & 0 & -n_x \\ -n_y & n_x & 0 \end{bmatrix}$ denotes the skew-symmetric matrix associated with \mathbf{n} . Substituting $\boldsymbol{\omega}$ into (24) yields:

$$\arg \min_{\boldsymbol{\omega}, \mathbf{t}} \sum_{i=1}^N \sum_{k' \in \mathcal{I}_i} \varphi^2(\hat{\mathbf{x}}_k, \mathcal{E}_i) \quad (26)$$

$$\text{s.t. } \boldsymbol{\omega}, \mathbf{t} \in \mathbb{R}^3, -\mathbf{R}^T \mathbf{t} \in \mathcal{U}, \quad (26a)$$

$$\sum_{k' \in \mathcal{M}} \|\hat{\mathbf{x}}_k - \mathbf{x}_k\|^2 \leq |\mathcal{M}| \cdot \epsilon^2, \quad (26b)$$

Then, Problem (26) can be solved by using nonlinear optimiza-

tion algorithms, such as the sequential quadratic programming (SQP) methods [37]. In this way, the optimal camera extrinsics, \mathbf{R}^* and \mathbf{t}^* , have been obtained simultaneously.

To reduce the computational complexity, $\forall 1 \leq i \leq N$, the projected contour point set \mathcal{I}_i can be approximately uniformly subsampled w.r.t. arc length to obtain $\mathcal{I}_i^{(\varsigma)}$, and in this case, only the points in $\mathcal{I}_i^{(\varsigma)}$ are used for back-projection and NLLS optimization. Let the sampling ratio be $0 < \varsigma \leq 1$, meaning that one point is sampled from \mathcal{I}_i every ς^{-1} points. With this subsampling strategy, the LC-VLP algorithm only requires replacing \mathcal{I}_i in (24) and (26) with $\mathcal{I}_i^{(\varsigma)}$. Note that as $\varsigma \rightarrow 0$, the number of optimization points decreases, which may lead to reduced optimization improvement, while the computational latency can be correspondingly reduced.

D. Complexity Analysis

We evaluate the computational overhead of the proposed LC-VLP algorithm by analyzing its theoretical time complexity. In the FreePnP stage, for each captured LED, both (11) and the reordering of \mathcal{I}_i require traversing all points in \mathcal{I}_i , resulting in a complexity of $\mathcal{O}(|\mathcal{I}_i|)$ for each operation. (16) and (15) sample M points from \mathcal{I}_i and \mathcal{E}_i to obtain \mathcal{I}_i^b and \mathcal{E}_i^b , respectively, each with a complexity of $\mathcal{O}(M)$. The above procedures are applied to all N captured LEDs, leading to an complexity of $\mathcal{O}(2\sum_{i=1}^N |\mathcal{I}_i| + 2MN)$ for constructing all approximate 3D–2D correspondences. Finally, (17) applies a PnP solver to the MN 3D–2D correspondences, with a complexity of $\mathcal{O}(MN)$. Overall, the time complexity of FreePnP is $\mathcal{O}(2\sum_{i=1}^N |\mathcal{I}_i| + 2MN) + \mathcal{O}(MN) = \mathcal{O}(\sum_{i=1}^N |\mathcal{I}_i| + MN)$.

In the refinement stage, the SQP method is employed to solve Problem (26). In each iteration, a total of $\sum_{i=1}^N |\mathcal{I}_i^{(\varsigma)}| = \varsigma \sum_{i=1}^N |\mathcal{I}_i|$ points are back-projected according to (22), resulting in a per-iteration complexity of $\mathcal{O}(\varsigma \sum_{i=1}^N |\mathcal{I}_i|)$. Moreover, since the dimension of the optimization objective $[\omega^T, \mathbf{t}^T]$ and the total number of constraints in (26a) and (26b) are both small constants, the per-iteration complexity of SQP itself can be regarded as a constant [38]. Therefore, the overall time complexity of solving (26) is $\mathcal{O}(\varsigma I \sum_{i=1}^N |\mathcal{I}_i|)$, where I denotes the number of iterations.

In conclusion, the time complexity of the proposed LC-VLP is expressed as $\mathcal{O}(\sum_{i=1}^N |\mathcal{I}_i| + MN) + \mathcal{O}(\varsigma I \sum_{i=1}^N |\mathcal{I}_i|) = \mathcal{O}(\varsigma I \sum_{i=1}^N |\mathcal{I}_i|)$, where $M < |\mathcal{I}_i| \ll \varsigma I |\mathcal{I}_i|$.

IV. SIMULATIONS AND EXPERIMENTS

In this section, we verify the performance and feasibility of our proposed LC-VLP algorithm via simulations and experiments. To quantitatively evaluate the positioning performance of LC-VLP and baselines, we respectively define the position error ε_p and rotation error ε_r as:

$$\varepsilon_p = \|\hat{\mathbf{x}} - \mathbf{x}\|, \quad (27)$$

$$\varepsilon_r = \frac{180}{\pi} \arccos \frac{1}{2} (\text{tr}(\hat{\mathbf{R}} \mathbf{R}^T) - 1), \quad (28)$$

where \mathbf{x} and $\hat{\mathbf{x}}$ denote the true and estimated positions, respectively, and \mathbf{R} and $\hat{\mathbf{R}}$ denote the corresponding rotation matrices. Based on these, we define the following metrics: (i) Mean of position/rotation errors (MPE/MRE); (ii) 50th/90th

TABLE I
SIMULATION PARAMETERS

Parameter		Value
Platform	Room size	$6 \text{ m} \times 8 \text{ m} \times 3 \text{ m}$
	LED semi-angle	$\Phi_{1/2} = 60^\circ$
	LED positions	$(2, 2, 3), (2, 6, 3), (4, 2, 3), (4, 6, 3)$
Camera	Focal lengths	$f_x = f_y = 800 \text{ px}$
	Principle point	$(u_0, u_0) = (320, 240) \text{ px}$
	Pixel physical size	$\delta x / \delta u = \delta y / \delta v = 1.25 \mu\text{m}/\text{px}$
LC-VLP	Sampling ratio	$\varsigma = 1$

percentile of position/rotation errors (P50/P90/R50/R90); and (iii) standard deviation (STD) of position errors.

The following algorithms are chosen as baselines:

- **V-PCA** [10], a SoTA algorithm based on circular LEDs. This method estimates the camera extrinsics and position using a purely geometric method, and requires at least two circular LEDs to be captured simultaneously.
- **VLC-PnP** [23], a SoTA algorithm based on rectangular LEDs. This method can estimate the camera pose using only a single LED; however, it relies on an additional magnetometer to assist in establishing the correct 3D–2D correspondences. In the simulations, we assume that there is no electromagnetic interference and the magnetometer measurements are perfectly accurate.
- **OPnP** [27], an advanced high-accuracy PnP solver. In the simulations, to enable the implementation of this method, four extra RPs are placed at the endpoints of the major and minor axes of each LED, respectively. This additional setup is not used by other baselines.

We note that, except for OPnP, other baselines are only applicable to a specific LED shape; therefore, they are included for comparison only in scenarios where LEDs of the corresponding shape are deployed. Moreover, to ensure a fair comparison, we consistently guarantee that at least two LEDs are fully captured by the camera.

A. Simulation Setup and Results

In the simulations, we consider a cuboid room in which four LEDs are installed at fixed positions on the ceiling. A camera with randomly generated position and orientation is used to capture the LEDs. To ensure the proper execution of positioning algorithms, the generated camera pose is always constrained such that at least two LEDs are visible. Unless otherwise specified, key system parameters are summarized in Table I. The camera image noise is modeled as a zero-mean white Gaussian noise with an STD of 2 px [10]. All statistical results in the simulations are averaged over 10,000 independent iterations to ensure universality.

1) *Homogeneous LED-Shape Scenarios*: We first consider scenarios where all LEDs share the same shape, with circular and rectangular LEDs taken as representative examples:

- *Scenario A*: Circular LEDs with a radius of 0.15 cm.
- *Scenario B*: Rectangular LEDs with a semi-major axis of 0.15 cm and a semi-minor axis of 0.12 cm.

Fig. 3 shows the cumulative distribution functions (CDFs) of the position and rotation errors for different algorithms. It

TABLE II
SIMULATION STATISTICAL RESULTS

Scenario	Algorithm	MPE [cm] ↓	P50 [cm] ↓	P90 [cm] ↓	STD [cm] ↓	MRE [°] ↓	R50 [°] ↓	R90 [°] ↓
Scenario A (Circular LEDs)	LC-VLP (Ours)	2.25	1.76	4.70	1.91	0.28	0.23	0.59
	V-PCA [10]	3.93	3.39	7.38	2.54	0.42	0.38	0.75
	OPnP [27]	5.21	3.50	10.82	8.79	0.65	0.50	1.36
Scenario B (Rectangular LEDs)	LC-VLP (Ours)	2.71	2.05	5.20	2.80	0.33	0.26	0.66
	VLC-PnP [23]	5.34	3.85	11.78	4.82	1.48	1.15	3.04
	OPnP [27]	6.08	4.07	14.51	9.43	0.75	0.58	1.62

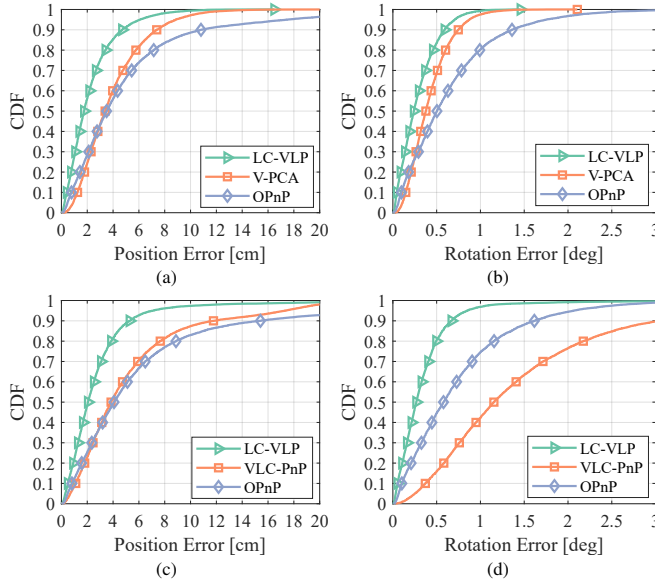


Fig. 3. The simulation CDFs of position and rotation errors. (a) and (b) are the results of Scenario A, while (c) and (d) are the results of Scenario B.

can be observed that, in both scenarios, LC-VLP consistently outperforms all baseline methods. Specifically, in Scenario A, LC-VLP achieves a 95th-percentile position accuracy of 6 cm and an 83rd-percentile rotation accuracy of 0.5°, whereas V-PCA only attains 82nd- and 70th-percentile accuracies, respectively. This performance gap arises because V-PCA is a purely geometric solution, whose accuracy and stability are inherently lower than those of the iterative optimization-based LC-VLP. The OPnP exhibits the largest errors, mainly because it does not exploit the fixed shape constraints among the RPs.

As shown in Figs. 3(c) and (d), in Scenario B, LC-VLP also achieves 93rd- and 80th-percentile position and rotation accuracies of 6 cm and 0.5°, respectively, which significantly outperforms VLC-PnP and OPnP. Note that although both VLC-PnP and OPnP are PnP-based methods, their performances differ, since OPnP is optimized for coplanar RPs, whereas VLC-PnP adopts a conventional PnP solver. When all RPs are coplanar, the latter is prone to accuracy degradation caused by depth ambiguity [27]. Therefore, although VLC-PnP applies nonlinear refinement, it remains more susceptible to large rotation errors. In contrast, LC-VLP incorporates not only the corner points but also the boundary points along LED edges into calculation. Therefore, compared with conventional PnP-based methods, this richer geometric constraint significantly improves both its accuracy and robustness.

The above simulation statistical results are summarized in

Table II. It can be observed that LC-VLP achieves MPEs of 2.25 cm and 2.71 cm in Scenarios A and B, respectively, corresponding to reductions of 43% and 49% compared with V-PCA and VLC-PnP. Likewise, in both scenarios, the MRE of LC-VLP is reduced by 25% and 78%, respectively, relative to V-PCA and VLC-PnP. In terms of positioning stability, LC-VLP consistently yields the lowest STD, indicating that it maintains a more balanced accuracy across different spatial locations and camera poses, thereby demonstrating superior robustness. Moreover, other metrics reported in Table II further confirm that LC-VLP outperforms other baselines in all aspects, exhibiting high accuracy and stability in both position and orientation estimation; hence, further details are omitted for brevity.

In Fig. 4, we investigate the impact of LED size and image noise on positioning performance. Note that when varying the LED size, the circular LED radius is no longer fixed in Scenario A, while in Scenario B the rectangular LED's major axis is fixed and the minor axis is treated as the variable. We can observe that, as the LED size increases, both position and rotation estimation errors of all algorithms consistently decrease; conversely, increasing image noise leads to higher errors for all methods. In particular, in Figs. 4(a) and (b), as the radius of the circular LED varies, the MPE of LC-VLP ranges from 7.48 cm to 1.62 cm. By comparison, the 2nd-best method, V-PCA, achieves an MPE ranging from 9.82 cm to 3.00 cm. In terms of rotation accuracy, LC-VLP attains an MRE between 0.92° and 0.20°, whereas the MRE of V-PCA varies from 1.00° to 0.32°. In Figs. 4(c) and (d), as the image noise increases, the MPE of LC-VLP gradually rises to 4.48 cm and the MRE increases to 0.56°. In contrast, V-PCA and OPnP are more sensitive to image noise, exhibiting noticeably larger increases in both position and rotation errors.

Figs. 4(e) and (f) illustrate the variations of MPE and MRE with respect to the LED semi-minor axis in Scenario B. As the semi-minor axis increases, the MPE of LC-VLP decreases from 8.13 cm to 2.03 cm, and its MRE decreases from 0.90° to 0.25°, which consistently achieve the best performance across different LED sizes. From Figs. 4(g) and (h), it can be observed that in Scenario B, as the image noise increases, the MPE of LC-VLP rises from 0 to 8.23 cm and the MRE increases from 0 to 0.96°. Nevertheless, LC-VLP exhibits the smallest error growth among all baselines. In contrast, although VLC-PnP achieves the 2nd-best position accuracy, its rotation error is higher than that of OPnP. Overall, both VLC-PnP and OPnP are consistently outperformed by LC-VLP.

We further consider the following scenario where LEDs of other common shapes are deployed:

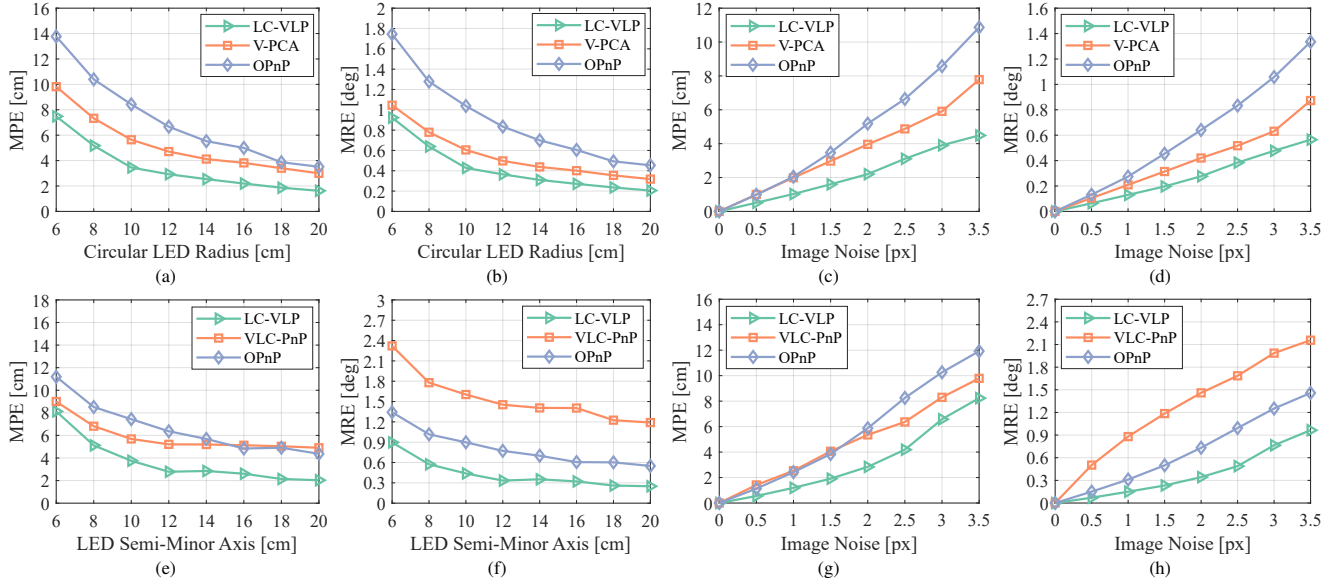


Fig. 4. The simulation results across different LED sizes and image noise STDs. (a)–(d) correspond to Scenario A: (a) and (b) show the MPE and MRE versus the LED radius, while (c) and (d) show the MPE and MRE versus the image noise. (e)–(h) correspond to Scenario B: (e) and (f) show the MPE and MRE versus the LED semi-minor axis, while (g) and (h) show the MPE and MRE versus the image noise.

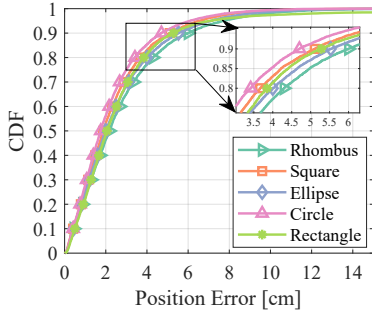


Fig. 5. The simulation results of LC-VLP across different LED shapes in Scenario C.

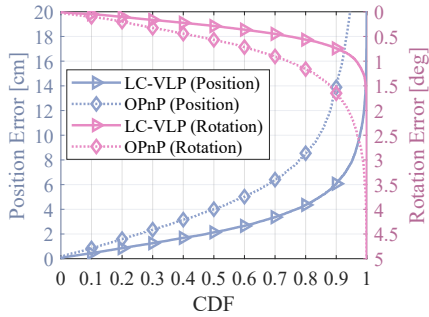


Fig. 6. The simulation results of LC-VLP and OPnP in Scenario D.

- *Scenario C*: Lamé curve LEDs with $\gamma = 1$ (rhombus or square) or $\gamma = 2$ (ellipse). Note that, in the square case, the LED's major and minor axes are identical to those in Scenario A; whereas in the rhombus or ellipse cases, the major and minor axes are identical to Scenario B.

In Fig. 5 we use CDFs to illustrate the impact of different LED shapes on the performance of LC-VLP under Scenario C. As shown, for rhombic, square, elliptical, circular, and rectangular LEDs, LC-VLP achieves MPEs of 2.80 cm, 2.41 cm,

2.60 cm, 2.23 cm, and 2.91 cm, respectively. These results indicate that, across Lamé curve-shaped LEDs with different γ 's, the MPE of LC-VLP consistently remains below 3 cm, and the performance variation among different LED shapes is relatively small. We note that square and circular LEDs yield higher accuracy than the other shapes, which is attributable to their larger areas in Scenario C. This observation is consistent with the results in Figs. 4(a), (b), (e), and (f), where larger LED areas are shown to improve the accuracy of LC-VLP.

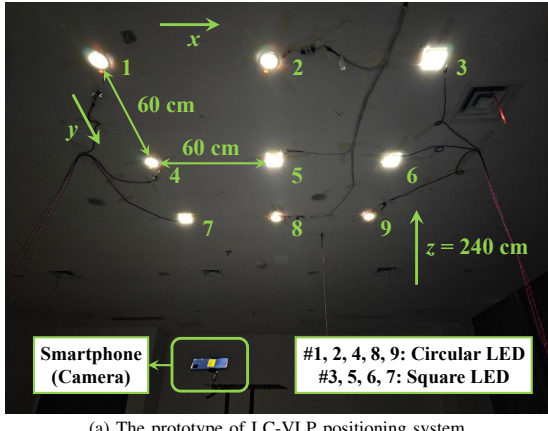
2) *Heterogeneous LED-Shape Scenarios*: In Section IV-A1, we simulated and compared the performance of different algorithms under homogeneous LED-shape scenarios. However, unlike V-PCA and VLC-PnP, the proposed LC-VLP is capable of achieving generic positioning when multiple LED shapes coexist in the environment. To evaluate this capability, we consider a complex scenario with heterogeneous LED layouts:

- *Scenario D*: Four LEDs with different shapes (rhombus, ellipse, circle, and rectangle as defined in Scenarios A–C) are deployed at the four LED positions listed in Table I.

Fig. 6 compares the position and rotation errors of LC-VLP and OPnP in Scenario D. As shown, LC-VLP achieves a 90th-percentile position accuracy of 6 cm and a 75th-percentile rotation accuracy of 0.5°. In terms of average performance, LC-VLP attains an MPE of 2.85 cm and an MRE of 0.35°, yielding an improvement of over 53% compared with OPnP. These results clearly demonstrate the superior positioning capability of the proposed LC-VLP in heterogeneous LED-shape scenarios.

B. Experimental Implementation

To further verify the feasibility of the proposed LC-VLP, we built an experimental platform, which is a heterogeneous LED-shape scenario. As shown in Fig. 7(a), the experiment was conducted in a cuboid space of size 2.4 m × 2.4 m × 2.4 m,



(a) The prototype of LC-VLP positioning system.

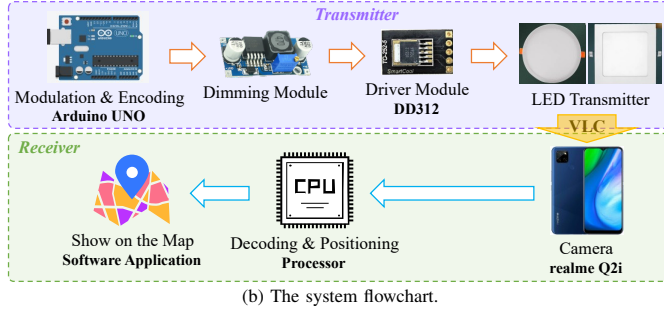


Fig. 7. The experimental implementation of LC-VLP.

TABLE III
EXPERIMENTAL PARAMETERS

Parameter		Value
LED	○	Semi-angle $\Phi_{1/2} = 67.5^\circ$ Power $P_t = 4 \text{ W}$ Radius $R_L = 3.4 \text{ cm}$ Positions (Height 240 cm) $(60, 60), (120, 60), (60, 120), (120, 180), (180, 180)$
	□	Semi-angle $\Phi_{1/2} = 67.5^\circ$ Power $P_t = 7 \text{ W}$ Edge length $D_L = 8.0 \text{ cm}$ Positions (Height 240 cm) $(180, 60), (120, 120), (180, 120), (60, 180)$
Camera	Model	Rear camera of realme Q2i
	Intrinsics	$f = 3.462 \text{ mm}$ $\delta x / \delta u = \delta y / \delta v = 1.12 \mu\text{m}/\text{px}$ $(u_0, u_0) = (2080, 1560) \text{ px}$
	Resolution	4160 px \times 3120 px
LC-VLP	Sampling ratio	$\varsigma = 1$

where a total of 9 circular (“○”) and square (“□”) LEDs are installed on the ceiling. The key experimental parameters are listed in Table III.

Fig. 7(b) illustrates the hardware block diagram of the proposed positioning prototype system. On the transmitter side, the control program is developed offline on a computer and deployed on an Arduino UNO development board. The LED ID is encoded using Manchester coding and modulated via on-off keying (OOK). A dimming module together with a DD312 driver module drives the LED to flicker at a high frequency, enabling the cyclic transmission of VLC packets containing the LED ID. On the receiver side, the prototype

employs the rear camera of a realme Q2i smartphone, which is a CMOS camera capable of receiving VLC signals through RSE while simultaneously capturing visual features such as LED contours. Specifically, the camera consecutively captures two frames within a very short time interval using a long (e.g., 6.67 ms) and a short exposure time (e.g., 1.25 ms), respectively. The former is used for extracting visual features, while the latter is used for decoding VLC information to obtain the LED IDs [10], [11]. Owing to the short inter-frame interval, the camera pose is typically assumed to remain unchanged between the two frames [10], [11]. These measurements are processed by a software application developed on the Android Studio to estimate the camera pose, with the results visualized in real time on a front-end interface such as a map view.

C. Experimental Results

To evaluate the impact of camera height and tilt angle on the performance of LC-VLP, the $2.4 \text{ m} \times 2.4 \text{ m}$ area was discretized into 25 grid points, and the smartphone camera was placed at each grid point to capture LED images for CPE. To ensure successful positioning, the camera was required to observe at least two LEDs at all times. When the camera is tilted about the x - or y -axis, fewer than two LEDs may be visible at certain grid points; such “unlocalizable” points are excluded from statistical analyses. Note that although these points cannot be localized under a specific tilt angle, they can become localizable under other tilt configurations. Therefore, according to the coverage theory [18], [39], these grid points are still considered to lie within the coverage area.

In Figs. 8(a) and (b), we first keep the camera horizontal and perform positioning at two different heights, i.e., 1.0 m and 1.4 m, to examine the effect of camera height on the performance of LC-VLP. To more clearly visualize the full 6-DoF camera poses, the top-view camera FoV cone representation in [40] is adopted. It can be observed that, compared with the results at 1.0 m, the estimated camera poses at 1.4 m are noticeably closer to the reference poses. Specifically, the MPEs at heights of 1.0 m and 1.4 m are 5.39 cm and 3.19 cm, respectively, while the corresponding MREs are 3.64° and 3.10° . These results indicate that the accuracy of LC-VLP improves as the camera height increases, which is because a higher camera captures larger LED images, which is equivalent to increasing the effective LED size. Enlarging the LED size can lead to higher accuracy, which is consistent with the simulation results. We also note that a lower camera height can increase the likelihood of observing more LEDs, which can partially mitigate the impact of image noise. However, in our experimental setup, the increase in the number of visible LEDs when lowering the camera height is limited; therefore, the LED size becomes the dominant influence factor.

In Figs. 8(c) and (d), the camera height is fixed at 1.4 m, while the camera is rotated by 30° about y - and x -axes, respectively. Together with Fig. 8(b), these results are used to evaluate the impact of camera tilt on the performance of LC-VLP. It can be observed that, under different tilt angles, the estimated camera poses remain closely aligned with the reference poses. Specifically, when the camera is rotated by

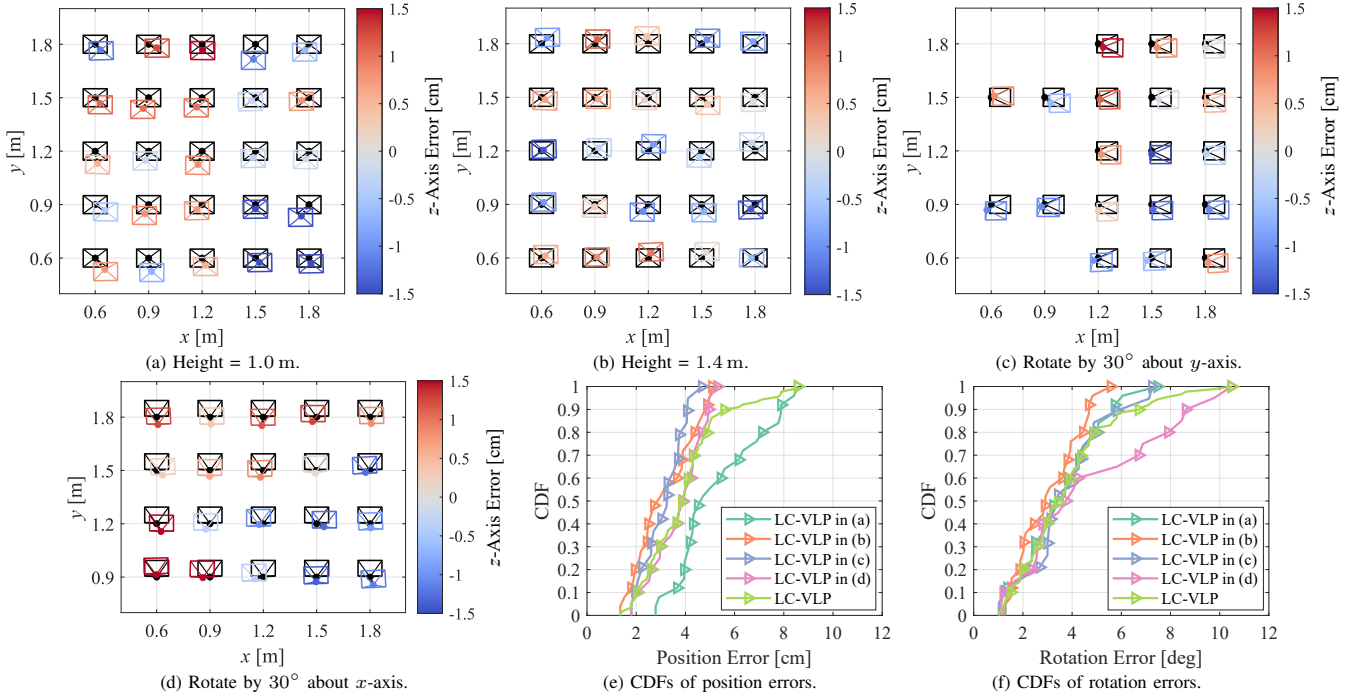


Fig. 8. The experimental results of LC-VLP. (a) and (b) show the estimated camera poses (top view) when the smartphone is placed horizontally at different heights; (c) and (d) show the estimated camera poses when the smartphone, positioned at a height of 1.4 m, is rotated about the x - and y -axes of WCS, respectively. Note that the black camera FoV cone denote the reference poses, while the colored cones represent the poses estimated by LC-VLP, where the color encodes the height difference along z -axis. Finally, (e) and (f) summarize the CDFs of position and rotation errors.

30° about y -and x -axes, the MPEs are 3.18 cm and 3.79 cm, respectively, while the corresponding MREs are 3.81° and 4.86°. These values are comparable to those obtained at the same height without rotation (3.19 cm and 3.10°), indicating that camera tilt has a limited impact on the performance of LC-VLP. It is worth noting that, compared with position, accurately determining the camera tilt angle is generally more challenging in practical setups. Consequently, the calibration of reference poses inevitably introduces additional uncertainty. As a result, the experimentally observed rotation errors are slightly larger than those reported in simulations.

Finally, the above results are summarized in Figs. 8(e) and (f). It can be observed that, across all experimental conditions, LC-VLP achieves an overall MPE of 3.94 cm and an MRE of 3.80°. These results demonstrate that LC-VLP can maintain high positioning accuracy and pose estimation accuracy under varying camera heights and different camera tilt angles.

V. CONCLUSION

In this paper, a generic LC-VLP algorithm has been proposed to enable high-accuracy full 6-DoF CPE in heterogeneous LED-shape scenarios. LC-VLP adopts a unified parametric modeling based on Lamé curves, which can represent a wide range of commonly-used LED shapes. With only the parameters of the captured Lamé curve-shaped LEDs, full 6-DoF CPE can be performed. Specifically, an LED database is constructed in advance to associate LED IDs with their corresponding curve parameters. When positioning, a back-projection strategy is introduced to formulate CPE as an NLLS optimization problem, where the algebraic distances

between back-projected points and the corresponding LED curves are iteratively minimized. To provide a reliable initialization, a FreePnP algorithm is further developed, which enables approximate pose estimation without requiring any pre-calibrated 3D–2D RP correspondences. The performance of LC-VLP has been verified through substantial simulations and experiments. In particular, simulation results show that LC-VLP outperforms SoTA methods in homogeneous LED-shape scenarios, achieving reductions of over 40% in position error and 25% in rotation error; experiments further show that LC-VLP can achieve an average position accuracy of less than 4 cm in a heterogeneous LED-shape scenario. Therefore, LC-VLP holds strong potential for deployment in real-world indoor positioning-enabled applications.

APPENDIX A PROOF OF THEOREM 1

Proof: Let the camera optical center in WCS be denoted by c . Consider three points with world coordinates \mathbf{x}_k , $k = 1, 2, 3$, and let the pixel coordinates of their corresponding projections on the image plane be \mathbf{u}_k^p .

(*Sufficiency*) Since the three points \mathbf{x}_k are collinear, there exists a non-zero scalar λ such that:

$$\mathbf{x}_1 - \mathbf{x}_2 = \lambda(\mathbf{x}_2 - \mathbf{x}_3). \quad (29)$$

Substituting (3) into (29) yields:

$$\begin{aligned} \mathbf{x}_1^c - \mathbf{x}_2^c &= \mathbf{R}(\mathbf{x}_1 - \mathbf{x}_2) + \mathbf{t} - \mathbf{t} = \lambda\mathbf{R}(\mathbf{x}_2 - \mathbf{x}_3) \\ &= \lambda((\mathbf{R}\mathbf{x}_2 + \mathbf{t}) - (\mathbf{R}\mathbf{x}_3 + \mathbf{t})) = \lambda(\mathbf{x}_2^c - \mathbf{x}_3^c), \end{aligned} \quad (30)$$

which shows that the points \mathbf{x}_k remain collinear in CCS, i.e., their camera coordinates \mathbf{x}_k^c are linearly dependent. Concatenating \mathbf{x}_k^c , $k = 1, 2, 3$ into a matrix, we have:

$$\det [\mathbf{x}_1^c, \mathbf{x}_2^c, \mathbf{x}_3^c] = 0. \quad (31)$$

Let s_k denote the z -coordinate of \mathbf{x}_k^c . By multiplying both sides of (31) by $\frac{1}{s_1 s_2 s_3}$, we obtain:

$$\det \left[\frac{1}{s_1} \mathbf{x}_1^c, \frac{1}{s_2} \mathbf{x}_2^c, \frac{1}{s_3} \mathbf{x}_3^c \right] = \frac{1}{s_1 s_2 s_3} \det [\mathbf{x}_1^c, \mathbf{x}_2^c, \mathbf{x}_3^c] = 0. \quad (32)$$

Furthermore, since the intrinsic matrix \mathbf{K} is invertible, multiplying $\det(\mathbf{K}^{-1})$ yields:

$$\det(\mathbf{K}^{-1}) \cdot \det \left[\frac{1}{s_1} \mathbf{x}_1^c, \frac{1}{s_2} \mathbf{x}_2^c, \frac{1}{s_3} \mathbf{x}_3^c \right] = 0. \quad (33)$$

Then from (2) we have:

$$\det [\tilde{\mathbf{u}}_1^p, \tilde{\mathbf{u}}_2^p, \tilde{\mathbf{u}}_3^p] = \det \left\{ \mathbf{K}^{-1} \left[\frac{1}{s_1} \mathbf{x}_1^c, \frac{1}{s_2} \mathbf{x}_2^c, \frac{1}{s_3} \mathbf{x}_3^c \right] \right\} = 0, \quad (34)$$

which means the $\tilde{\mathbf{u}}_k^p$, $k = 1, 2, 3$ are linearly dependent, i.e., there exist $\lambda_2 \lambda_3 \neq 0$ such that $\tilde{\mathbf{u}}_1^p + \lambda_2 \tilde{\mathbf{u}}_2^p + \lambda_3 \tilde{\mathbf{u}}_3^p = \mathbf{0}$. Since $\tilde{\mathbf{u}}_k^p = [(\mathbf{u}_k^p)^\top, 1]^\top$, we also have:

$$\left\{ \begin{array}{l} \mathbf{u}_1^p + \lambda_2 \mathbf{u}_2^p + \lambda_3 \mathbf{u}_3^p = \mathbf{0}, \\ 1 + \lambda_2 + \lambda_3 = 0, \end{array} \right. \quad (35a)$$

$$\left\{ \begin{array}{l} \mathbf{u}_1^p + \lambda_2 \mathbf{u}_2^p + \lambda_3 \mathbf{u}_3^p = \mathbf{0}, \\ 1 + \lambda_2 + \lambda_3 = 0, \end{array} \right. \quad (35b)$$

which clearly shows the collinearity of the projected points \mathbf{u}_k^p , $k = 1, 2, 3$ in PCS.

(Necessity) Since the projected points \mathbf{u}_k^p , $k = 1, 2, 3$ are collinear in PCS, we have (35), and we can still backtrack the above procedure up to (31). (31) shows the linear dependency of \mathbf{x}_k^c , which means there exist $\alpha_1 \alpha_2 \alpha_3 \neq 0$ such that:

$$\alpha_1 \mathbf{x}_1^c + \alpha_2 \mathbf{x}_2^c + \alpha_3 \mathbf{x}_3^c = \mathbf{0}. \quad (36)$$

Substituting (3) into (36), we have:

$$\alpha_1 \mathbf{x}_1 + \alpha_2 \mathbf{x}_2 + \alpha_3 \mathbf{x}_3 = -(\alpha_1 + \alpha_2 + \alpha_3) \mathbf{R}^\top \mathbf{t}. \quad (37)$$

According to (4), the world coordinates of the camera optical center are $\mathbf{c} = -\mathbf{R}^\top \mathbf{t}$, which can be substituted into (37):

$$\alpha_1 \mathbf{x}_1 + \alpha_2 \mathbf{x}_2 + \alpha_3 \mathbf{x}_3 - (\alpha_1 + \alpha_2 + \alpha_3) \mathbf{c} = \mathbf{0}. \quad (38)$$

This implies that if $\sum_{k=1}^3 \alpha_k \neq 0$, then \mathbf{x}_k , $k = 1, 2, 3$ and \mathbf{c} are always coplanar. Since there exists a plane that contains \mathbf{x}_k , $k = 1, 2, 3$, but does not contain \mathbf{c} , it should hold that $\sum_{k=1}^3 \alpha_k = 0$ which yields:

$$\mathbf{x}_1 - \mathbf{x}_3 = -\frac{\alpha_2}{\alpha_1} (\mathbf{x}_2 - \mathbf{x}_3). \quad (39)$$

This clearly demonstrates the collinearity of points \mathbf{x}_k , $k = 1, 2, 3$ in WCS. Theorem 1 is proved. \square

APPENDIX B PROOF OF PROPOSITION 1

Proof: To prove Proposition 1, it suffices to show that the arc-length differential ds of the projected curve is approximately proportional to the polar-angle differential $d\theta$ along the original LED boundary curve.

For simplicity, we assume that the LED center is located at the origin of WCS (equivalently, CyCS), and its $\phi = 0$. We consider a point on the LED boundary curve parameterized by the polar angle θ . Its coordinates in CCS are obtained from

WCS via the transformation $\zeta(\theta)$. Moreover, we define the projection function $\varpi(\mathbf{x}^c)$ that maps a point in CCS onto PCS. These two mappings are respectively given by:

$$\left\{ \begin{array}{l} \zeta(\theta) = \mathbf{R}\rho(\theta)\psi(\theta) + \mathbf{t}, \\ \varpi(\mathbf{x}^c) = \frac{f}{z^c} \begin{bmatrix} x^c \\ y^c \end{bmatrix} + \begin{bmatrix} u_0 \\ v_0 \end{bmatrix} \end{array} \right. \quad (40a)$$

$$\left\{ \begin{array}{l} \zeta(\theta) = \mathbf{R}\rho(\theta)\psi(\theta) + \mathbf{t}, \\ \varpi(\mathbf{x}^c) = \frac{f}{z^c} \begin{bmatrix} x^c \\ y^c \end{bmatrix} + \begin{bmatrix} u_0 \\ v_0 \end{bmatrix} \end{array} \right. \quad (40b)$$

It follows that the projected LED curve can be written as $s = \varpi(\zeta(\theta))$. By applying the chain rule, we directly differentiate s with respect to θ , yielding:

$$\begin{aligned} \frac{ds}{d\theta} &= \frac{1}{d\theta} d\varpi(\zeta(\theta)) = \frac{d\varpi}{d\zeta} \cdot \frac{d\zeta}{d\theta} \\ &= \frac{f}{z^c} \begin{bmatrix} 1 & 0 & \frac{-x^c}{z^c} \\ 0 & 1 & \frac{-y^c}{z^c} \end{bmatrix} \cdot \mathbf{R} \begin{bmatrix} \frac{d\rho}{d\theta} \cos \theta - \rho \sin \theta \\ \frac{d\rho}{d\theta} \sin \theta + \rho \cos \theta \\ 0 \end{bmatrix} \\ &\triangleq \frac{f}{z^c} \mathbf{\Xi} \cdot \mathbf{R}\rho. \end{aligned} \quad (41)$$

Therefore, we have:

$$\left\| \frac{ds}{d\theta} \right\| \leq \frac{f}{z^c} \|\mathbf{\Xi}\|_2 \cdot \|\mathbf{R}\rho\| = \frac{f}{z^c} \|\mathbf{\Xi}\|_2 \cdot \|\rho\|, \quad (42)$$

where

$$\|\mathbf{\Xi}\|_2 = \sqrt{\max_{\|\mathbf{y}\|=1} \mathbf{y}^\top \mathbf{\Xi} \mathbf{y}} \quad (43)$$

denotes the 2-norm of $\mathbf{\Xi}$. Let the unit vector $\mathbf{y} = [y_1, y_2]^\top$, then we have:

$$\begin{aligned} \mathbf{y}^\top \mathbf{\Xi} \mathbf{y} &= y_1^2 + y_2^2 + \left(-y_1 \cdot \frac{x^c}{z^c} - y_2 \cdot \frac{y^c}{z^c} \right)^2 \\ &\leq 1 + (y_1^2 + y_2^2) \left(\left(\frac{x^c}{z^c} \right)^2 + \left(\frac{y^c}{z^c} \right)^2 \right) \\ &= 1 + \left(\frac{x^c}{z^c} \right)^2 + \left(\frac{y^c}{z^c} \right)^2. \end{aligned} \quad (44)$$

Furthermore, since the LED is captured by the camera, it must lie within the camera's field of view (FoV). This leads to the following constraints:

$$\left\{ \begin{array}{l} 0 \leq \frac{|x^c|}{z^c} \leq \tan \alpha_x, \\ 0 \leq \frac{|y^c|}{z^c} \leq \tan \alpha_y, \end{array} \right. \quad (45a)$$

$$\left\{ \begin{array}{l} 0 \leq \frac{|x^c|}{z^c} \leq \tan \alpha_x, \\ 0 \leq \frac{|y^c|}{z^c} \leq \tan \alpha_y, \end{array} \right. \quad (45b)$$

which can then be substituted into (43) and (44), resulting in:

$$\|\mathbf{\Xi}\|_2 \leq \sqrt{1 + \tan^2 \alpha_x + \tan^2 \alpha_y} \triangleq \Omega_{\text{FoV}}. \quad (46)$$

Substituting (46) into (42), we obtain that the objective ratio $\frac{ds}{d\theta}$ satisfies:

$$\begin{aligned} \frac{ds}{d\theta} &= \left\| \frac{ds}{d\theta} \right\| \leq \frac{f}{z^c} \Omega_{\text{FoV}} \|\rho\| \\ &= \frac{f}{z^c} \Omega_{\text{FoV}} \sqrt{\left(\frac{d\rho}{d\theta} \right)^2 + \rho^2} = \frac{f}{z^c} \Omega_{\text{FoV}} \frac{d\rho}{d\theta}. \end{aligned} \quad (47)$$

We can observe that $\frac{d\rho}{d\theta}$ corresponds exactly to the arc-length differential of the original LED curve in WCS, which naturally

satisfies:

$$\int_0^{2\pi} \frac{d\ell}{d\theta} d\theta = L, \quad \frac{d\ell}{d\theta} > 0, \quad (48)$$

where L denotes the perimeter of the LED. This implies that the arc-length differential $\frac{d\ell}{d\theta}$ is bounded, nonnegative, and varies smoothly with respect to θ .

Moreover, in typical indoor positioning scenarios, it holds that $f\Omega_{\text{FoV}} \ll z^c$, since $f\Omega_{\text{FoV}}$ is typically at the millimeter/centimeter scale, whereas z^c is usually at the meter scale. Substituting this condition into (47), we observe that $\frac{ds}{d\theta}$ also varies slowly with θ . Consequently, the projected arc-length differential ds is approximately proportional to the polar-angle differential $d\theta$. Proposition 1 is proved. \square

REFERENCES

- [1] Y. Yang *et al.*, “Positioning using wireless networks: Applications, recent progress, and future challenges,” *IEEE J. Sel. Areas Commun.*, vol. 42, no. 9, pp. 2149–2178, Sep. 2024.
- [2] Z. Yao, Y. Qi, and M. Lu, “Subcarrier modulated navigation signal processing in GNSS: A review,” *Satell. Navig.*, vol. 5, p. 24, 2024.
- [3] H. Yu *et al.*, “Floor-plan-aided indoor localization: Zero-shot learning framework, data sets, and prototype,” *IEEE J. Sel. Areas Commun.*, vol. 42, no. 9, pp. 2472–2486, Sep. 2024.
- [4] W. Pan, Y. Yang, M. Chen, D. Wei, C. Guo, and S. Mao, “Fusing Bluetooth with pedestrian dead reckoning: A floor plan-assisted positioning approach,” 2025, *arXiv:2504.09905*.
- [5] Q. Wang *et al.*, “Parallel deep learning for NLOS detection and error mitigation in UWB positioning,” *IEEE Internet Things J.*, vol. 12, no. 20, pp. 43 571–43 587, Oct. 2025.
- [6] J. Xu *et al.*, “The principle, methods and recent progress in RFID positioning techniques: A review,” *IEEE J. Radio Freq. Identificat.*, vol. 7, pp. 50–63, 2023.
- [7] S. Xu, Y. Zheng, S. Xing, and Y. Wu, “Simultaneous position and orientation estimation in single optical IRS-assisted visible light systems using single LED and single PD,” *IEEE Internet Things J.*, vol. 12, no. 19, pp. 41 181–41 196, Oct. 2025.
- [8] H. Shi, C. Wang, and Y. Zhao, “Visible light positioning using a single LED and a single rotatable photodetector,” *IEEE Photon. Technol. Lett.*, vol. 37, no. 18, pp. 1033–1036, Sep. 2025.
- [9] D. Su, X. Wang, S. Liu, and W. Ding, “Four-dimensional indoor visible light positioning: A deep-learning-based perspective,” *J. Frankl. Inst.*, vol. 360, no. 6, pp. 4071–4090, Apr. 2023.
- [10] Z. Zhu, C. Guo, R. Bao, M. Chen, W. Saad, and Y. Yang, “Positioning using visible light communications: A perspective arcs approach,” *IEEE Trans. Wirel. Commun.*, vol. 22, no. 10, pp. 6962–6977, Oct. 2023.
- [11] Z. Zhu, Y. Yang, M. Chen, C. Guo, J. Hao, and S. Cui, “Visible light positioning with visual odometry: A single luminaire based positioning algorithm,” *IEEE Trans. Commun.*, vol. 72, no. 8, pp. 4978–4991, Aug. 2024.
- [12] J. He, N. Huang, and C. Gong, “Indoor 3D visible light positioning based on multiple cameras: Algorithm design and error analysis,” *IEEE Trans. Wirel. Commun.*, vol. 23, no. 5, pp. 4331–4346, May 2024.
- [13] W. Pan, Y. Yang, D. Wei, M. Zhang, and Z. Zhu, “Passive multi-target visible light positioning based on multi-camera joint optimization,” *IEEE Commun. Lett.*, vol. 29, no. 10, pp. 2421–2425, Oct. 2025.
- [14] Z. Zhu, Y. Yang, M. Chen, C. Guo, J. Cheng, and S. Cui, “A survey on indoor visible light positioning systems: Fundamentals, applications, and challenges,” *IEEE Commun. Surv. Tut.*, vol. 27, no. 3, pp. 1656–1686, Jun. 2025.
- [15] S. Bastiaens, M. Alijani, W. Joseph, and D. Plets, “Visible light positioning as a next-generation indoor positioning technology: A tutorial,” *IEEE Commun. Surv. Tut.*, vol. 26, no. 4, pp. 2867–2913, 4th Quart. 2024.
- [16] Z. Li, J. Shi, C. Shen, Y. Zhang, J. Zhang, and N. Chi, “Adaptive visible light integrated sensing and communication for cable-free virtual reality,” *Photon. Res.*, vol. 13, no. 9, pp. 2453–2463, Sep. 2025.
- [17] Y.-S. Kuo, P. Pannuto, K.-J. Hsiao, and P. Dutta, “Luxapose: indoor positioning with mobile phones and visible light,” in *Proc. 20th Annu. Int. Conf. Mob. Comput. Netw. (MobiCom)*, Maui, HI, USA, Sep. 2014, pp. 447–458.
- [18] F. He *et al.*, “Inertial sensor-assisted high-coverage visible light positioning algorithm,” *IEEE Photon. J.*, vol. 16, no. 3, p. 6802008, Jun. 2024.
- [19] R. Zhang, W.-D. Zhong, Q. Kemao, and S. Zhang, “A single LED positioning system based on circle projection,” *IEEE Photon. J.*, vol. 9, no. 4, p. 7905209, Aug. 2017.
- [20] H. Cheng, C. Xiao, Y. Ji, J. Ni, and T. Wang, “A single LED visible light positioning system based on geometric features and CMOS camera,” *IEEE Photon. Technol. Lett.*, vol. 32, no. 17, pp. 1097–1100, Sep. 2020.
- [21] X. Liu, Y. Gao, X. Wang, L. Guo, and X. Wei, “Cognitive indoor positioning using sparse visible light source,” *IEEE Trans. Computat. Social Syst.*, vol. 9, no. 6, pp. 1682–1692, Dec. 2022.
- [22] L. Bai *et al.*, “Computer vision-based localization with visible light communications,” *IEEE Trans. Wirel. Commun.*, vol. 21, no. 3, pp. 2051–2065, Mar. 2022.
- [23] B. Hussain, Y. Wang, R. Chen, and C. P. Yue, “Camera pose estimation using a VLC-modulated single rectangular LED for indoor positioning,” *IEEE Trans. Instrum. Meas.*, vol. 71, p. 8505511, 2022.
- [24] C. Yang, S. Wen, D. Yuan, J. Chen, J. Huang, and W. Guan, “CGA-VLP: High accuracy visible light positioning algorithm using single square LED with geomagnetic angle correction,” *Photonics*, vol. 9, no. 9, p. 653, Sep. 2022.
- [25] S. Zhang, P. Du, H. Yang, R. Zhang, C. Chen, and A. Alphones, “Recent progress in visible light positioning and communication systems,” *IEICE Trans. Commun.*, vol. E106-B, no. 2, pp. 84–100, Feb. 2023.
- [26] V. Lepetit, F. Moreno-Noguer, and P. Fua, “EPnP: An accurate $O(n)$ solution to the PnP problem,” *Int. J. Comput. Vis.*, vol. 81, no. 2, pp. 155–166, Feb. 2009.
- [27] Y. Zheng, Y. Kuang, S. Sugimoto, K. Åström, and M. Okutomi, “Revisiting the PnP problem: A fast, general and optimal solution,” in *IEEE Int. Conf. Comput. Vis. (ICCV)*, Sydney, NSW, Australia, Dec. 2013, pp. 2344–2351.
- [28] L. Bai, Y. Yang, C. Feng, and C. Guo, “Received signal strength assisted perspective-three-point algorithm for indoor visible light positioning,” *Opt. Exp.*, vol. 28, no. 19, pp. 28 045–28 059, Sep. 2020.
- [29] S. C. Narasimman and A. Alphones, “Indoor visible light positioning for a single partially visible LED,” *IEEE Sens. Lett.*, vol. 8, no. 5, p. 6004504, May 2024.
- [30] S. Kajikawa, T. Oda, K. Takenaga, and K. Ichii, “Cladding shape fitting model for multi-core fibers using a Lamé curve,” *Opt. Exp.*, vol. 33, no. 20, pp. 42 756–42 767, Oct. 2025.
- [31] B. Ni, I. Elishakoff, C. Jiang, C. M. Fu, and X. Han, “Generalization of the super ellipsoid concept and its application in mechanics,” *Appl. Math. Model.*, vol. 40, no. 21, pp. 9427–9444, Nov. 2016.
- [32] M. Matsuura, “Gielis’ superformula and regular polygons,” *J. Geom.*, vol. 106, pp. 383–403, Mar. 2015.
- [33] P. Sturm, “Pinhole camera model,” in *Computer Vision: A Reference Guide*, 2nd ed., K. Ikeuchi, Ed. Boston, MA, USA: Springer, 2021, pp. 983–986.
- [34] X.-Y. Gong, H. Su, D. Xu, Z.-T. Zhang, F. Shen, and H.-B. Yang, “An overview of contour detection approaches,” *Int. J. Autom. Comput.*, vol. 15, pp. 656–672, Dec. 2018.
- [35] G. Guennebaud and M. Gross, “Algebraic point set surfaces,” *ACM Trans. Graph.*, vol. 26, no. 3, p. 23, Jul. 2007.
- [36] A. G. Valdenebro, “Visualizing rotations and composition of rotations with the Rodrigues vector,” *Eur. J. Phys.*, vol. 37, no. 6, p. 065001, Aug. 2016.
- [37] P. E. Gill, W. Murray, and M. A. Saunders, “SNOPT: An SQP algorithm for large-scale constrained optimization,” *SIAM Rev.*, vol. 47, no. 1, pp. 99–131, 2005.
- [38] Y. Aoyama, O. So, A. D. Saravatos, and E. A. Theodorou, “Second-order constrained dynamic optimization,” 2025, *arXiv:2409.11649*.
- [39] L. Bai, Y. Yang, Z. Zhang, C. Feng, C. Guo, and J. Cheng, “A high-coverage camera assisted received signal strength ratio algorithm for indoor visible light positioning,” *IEEE Trans. Wirel. Commun.*, vol. 20, no. 9, pp. 5730–5743, Sep. 2021.
- [40] J. Kang, “Retraining-free camera localization in indoor point clouds using edges and normals,” *IEEE Trans. Instrum. Meas.*, vol. 74, p. 7511811, 2025.